EXPERIMENTAL INVESTIGATION OF DYNAMIC STALL

G. Pailhas, R. Houdeville, Ph. Barricau
Aerodynamics and Energetics Models Department
A. Le Pape, A. Faubert
Applied Aerodynamics Department
Ph. Loiret
Fauga-Mauzac Wind Tunnels Department
F. David
Structural Dynamics and Coupled Systems Department
ONERA, BP 72, 92322 Châtillon Cedex, France

Abstract

The flow field above an OA209 airfoil, periodically oscillated under dynamic stall conditions was experimentally studied. The airfoil was pitched sinusoidally for various mean angles and amplitudes covering a range of angles of attack between 3° to 20°. Two configurations representative of typical dynamic stall environment (Deep and Moderate Stall) were produced. Effect of reduced frequency, amplitude of the pitching motion and of nominal incidence on lift dynamic and moment variation was analyzed from unsteady pressure measurements. The periodic features of the mean and turbulent velocity fields have been explored by use of LDV. PIV technique was applied to get information of the unsteady flow in enlarged measurement planes above the airfoil and in the wake to analyze the mechanism involved in dynamic stall through instantaneous velocity field. The local skin friction was measured in an attempt to determine the nature of the boundary layer separation leading up to dynamic stall.

Notation

x	chordwise coordinate from the leading edge
y	vertical coordinate
z	coordinate in spanwise direction
U_∞	reference streamwise velocity
U_e	external boundary layer velocity
c	chord length
f	frequency of oscillating wing
k	reduced frequency, $\omega c/2U_\infty$; $\omega = 2\pi f$
α	angle of attack, deg
α_0	mean angle, deg
$\Delta\alpha$	amplitude, deg
Cm	pitching–moment coefficient
Cz	normal force coefficient
ρ	density
μ	dynamic viscosity
τ_w	wall shear stress
Cf_{local}	skin friction coefficient, $2\tau_w/\rho_e U_e^2$

Introduction

"Dynamic Stall" flow phenomenon describes the delay of stall on wings and aircraft that are rapidly pitched beyond the static stall angle. Helicopters rotor blades, fighter aircraft, wind turbines or jet engines are closely concerned by this phenomenon. The mechanisms of stall onset are extremely complex depending on many parameters as Reynolds and Mach numbers, leading edge radius, sweep, etc. Therefore, they include various flow problems like flow unsteadiness, compressibility, transition, turbulence or 3D effects. In steady flow, the angle of attack for which stall occurs depends essentially upon the geometry of the wing and weakly upon the Reynolds number. If the airfoil undergoes rapid pitch-up, the flow differs significantly from that of the same airfoil moved slowly through the same range of angles [1]. During rapid pitch, the predominant feature of dynamic stall is the formation and the shedding of a spanwise vortex-like disturbance from the leading edge region. Transient forces and moments are fundamentally different from steady case. The lift climbs beyond the angle for which the steady airfoil stalls. As the vortex propagates, the flow separates on the upper surface of the airfoil. Then, a substantial loading hysteresis and a time-dependant moment occur [2] before the starting of a new oscillating cycle.

The aerodynamics of helicopter rotor blades is strongly affected by unsteady phenomena present in

the retreating-blade side of the rotor. As a result, periodic flow separation and reattachment occur during blades revolution, which may lead, under certain circumstances, to dynamic stall phenomenon characterized by abrupt fluctuations of aerodynamic forces which can seriously limit the helicopter performance. Large induced vibratory loads may degenerate morever to aeroelastic instabilities such as stall flutter. Such phenomena that limit for example the flight envelope of the helicopter have been studied for many years as an important practical problem. Efforts have been done to prevent sufficiently early their critical apparition in the goal of suppressing them. The simplification of the basic 3D unsteady problem has been suggested by many authors. Hama [3] justified the mainly 2D character of stall on retreating blade disregarding three-dimensional and centrifugal effects. Mc Croskey et Fisher [4] reduced the experimental study of dynamic stall on helicopter rotor to the analysis of the flow on an oscillating blade. They showed the remarkable similarity in results between the airfoil oscillating sinusoidally in pitch and a rotating rotor blade. As it is widely accepted that the unsteady fluid mechanisms developing on a rotor blade can be reasonably well simulated by an airfoil oscillating in pitch at an incidence sufficiently above the static stall limit, the present study is devoted to provide a detailed and coherent database for numerical simulations.

The specific objectives of the present experiment were:

- to analyze the general effects of the vortex shedding phenomenon in the cases of dynamic stalls, qualified as “deep” or “moderate” according to the behavior of the aerodynamic coefficients. As these coefficients are deduced from pressure measurement, a particular attention is devoted to the critical analysis of pressure measurement accuracy and tests repeatability.
- to document the global flow over the airfoil and in the wake using LDV and PIV measurements.
- to capture surface flow details using thin hot films sensors and skin friction gauges to identify separated areas.

Description of the experimental set-up

F2 subsonic Wind Tunnel

The experiments were conducted in the F2 subsonic wind tunnel. This research facility is a continuous wind tunnel with a rectangular test section size 1.4 meters wide by 1.8 meters high and 5 m long. The wind tunnel is designed to perform tests varying the velocity from 0 to 100 $m.s^{-1}$. The side walls of the test section are equipped with removal glass panels which allow viewing access to be specially adapted to the requirements of each test. A view of the model in the F2 wind tunnel test section is presented in Figure 1.

Figure 1: View of the model in F2 wind tunnel

The OA209 model

The rectangular plan form model is an OA209 airfoil of 0.50 m chord and 1.40 m span mounted horizontally in the F2 wind tunnel. The model is oscillated sinusoidally in pitch about the quarter of the chord. It is made of two carbon skins stuck together and containing polyurethane material of low density. The airfoil is supported at both ends by two rods (4.50 cm diameter) each of which passes through the lateral glass walls of the test section and are held up by a pair of cylindrical bearings housed in an external support fixed on the test section frame.

Oscillatory Drive mechanism

The pitch drive system generates a sinusoidal pitching motion about the quarter chord. The pitching mechanism consists of a Parvex HX820VR motor coupled to an endless screw speed-reducing system. The alternate rotative movement is transmitted without modification to the right rod of the model by the way of a four lever arm mechanism. A linear encoder connected to each airfoil support rod provides the instantaneous incidence angle. A motion control board in a PC controls the execution of the pitching motion. The sinusoidal movement of the model is permanently watched closely during the experiment.

The difference between the actual and the imposed incidence angle does not exceed 0.04° during a measurement test of four hours long. The uncertainty on the model incidence was estimated to be less than 0.09°.

Instrumentation

Pressure transducers – The airfoil is equipped with 55 pressure taps distributed on the upper and lower sides; 15 of them are concentrated in leading edge region. A set of 40 Kulite miniature pressure transducers type XCKL093-5D for dynamic pressure measurement were used. They have a maximum pressure range of 5 psi. These sensors are small enough to be located inside the model and coupled closely to the pressure taps so that their natural frequency, with wing orifice of 0.75 mm, was 20 kHz. The pressure transducers were calibrated in situ; their response to a known sinusoidal pressure was recorded to take into account amplitude attenuation and phase shift due to the tubing length effect.

Hot film sensors – They consist of TAO SYSTEMS thin plastic foil (0.002 in.) on which the multi-element hot-film sensor array is deposited. The hot film sensors are stuck on a thermal isolating material moulded on a cavity machined on the model and are perfectly flushing the wall. From X/c = 0.07 to X/c = 0.36, 20 closely spaced hot-film sensors are distributed over the upper surface. Sets of 12 sensors from X/c = 0.75 to X/c = 0.89 are mounted on the lower surface of the airfoil. The gauges were connected to a bank of house-made constant temperature anemometers. They were operated at an overheat ratio of 1.8.

Skin friction gauges – These in-house built gauges are conceived to measure skin friction in separated regions where the friction is small and the flow unsteady by nature. The proposed gauge (figure 2) is a cylindrical body made of plexiglass, 5 mm in diameter and 6 mm high.

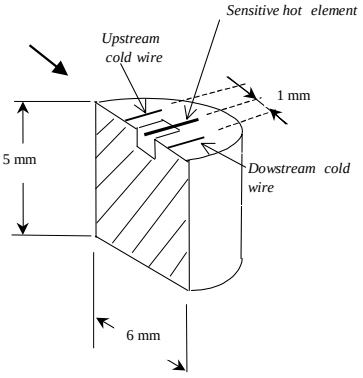

Figure 2: Half view of the three wire gauge

The sensitive element is a quartz fiber supporting a thin conductive layer. A square cavity is provided in the gauge body under the fiber to minimize the thermal leakage to the substrate. To eliminate the ambiguity of the algebraic sign of τ_w, two temperature measurement wires are added on either side of the hot element of the gauge (figure 2) to give information on the direction of the fiber wake. A constant-current bridge supplies each cold wire. The signals are digitized and the temperatures of the cold wires are compared to fixed thresholds to get the sign of the friction.

Nine friction gauges were incorporated in the upper surface of the model from X/c = 0.05 to X/c = 0.85 at span location Z/c = 0.60.

Accelerometers – Two accelerometers were located inside the model (one in the leading edge region, the other in the trailing edge region) to control its deformation during the experiment.

Thermocouple - An IT-23 hypodermic thermocouple (0.07mm diameter) was put in the isolating support of the hot films flushing the wall. The temperature of the wing is used to correct the tensions delivered by film and hot wire sensors.

Experimental procedure

The static pressure distributions over the upper and lower surfaces were measured varying incidence angle from 0° to about 16° which is roughly the static stall incidence. Simultaneously, at each incidence angle, a survey of the velocity profile in the wake at the station X/c = 0.5 downstream the airfoil was undertaken by LDV. Static drag and lift coefficients were then obtained.

For dynamic analysis, the angle of attack of the airfoil was varied as $\alpha = \alpha_0 + \Delta\alpha \sin(2\pi ft)$. The individual effects of α_0, $\Delta\alpha$ and f on the flow field through the time dependent component of the lift and moment coefficients were at first analyzed. This parametric analysis was conducted varying successively each parameter and fixing the two others. Two configurations representative of two typical dynamic stall environment ("Deep" and "Moderate " Stall) were selected to be more deeply investigated.

The dynamic data, consisting of 40 pressure transducers, 32 hot-film gauges, 9 skin friction gauges and their 18 associated cold wires, a linear encoder and 2 accelerometers had to be acquired on three groups of 32 channels available on the data acquisition system. The 96 signals were simultaneously sampled and hold amplified. Sampling rate of 2.0 KHz was used for a total of 2048 samples/channel. A number of repeated data acquisition sequences (from 50 to 300 cycles) were carried out for evaluation of average results. These large sampled sets of data allowed us, in the case of an oscillation frequency of 7 Hz, to get averaged values from about 1500 samples. Data acquisition was triggered from an external TTL trigger generated when the encoder gives, in the rising slope of its signal, the nominal incidence value of the model. The data were analyzed using either the ensemble averaged values or the phase averaged

values. Each data run was preceded by the acquisition sequence of wind-off zeros for all channels.

Experimental conditions

Experiments were conducted at a chord Reynolds number Re=1.8 10^6 with a reference velocity $U_\infty \cong 55$ ms^{-1}. Unsteady loads and moments were measured for the following conditions:

α_0: 6° - 13°
$\Delta\alpha$: 3° - 7°
k: 0.05 – 0.20 ($k=\pi fc/U_\infty$)

Detailed measurements and analysis are done, however, for only one reduced frequency k=0.10.

Static pressure survey

Static pressures were first measured: Figure 3 shows the lift coefficient obtained from wall pressure integration during the preliminary campaign and the second detailed campaign. One can first notice the very good repeatability of the measurements. The lift coefficient polar also shows a very sharp stall occurring around 16^o at the Reynolds number equal to 1.8 10^6; in an interval of 0.1 degree, the lift coefficient Cz is falling from 1.45 to 0.9.

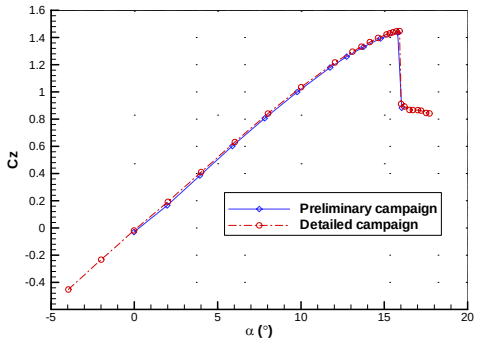

Figure 3: Static experimental lift coefficient of the OA209

Dynamic pressure survey

As described above, each dynamic pressure acquisition bloc corresponds to 2048 samples with a sampling rate of 2.0 kHz and for each test point several blocs are acquired (from 50 to 300) allowing to get numerous instantaneous oscillation cycles per test point. The aerodynamic coefficients were obtained by pressure integration at each instant. A particular attention was devoted to the integration by adding parabolic interpolations around the leading and trailing edges and drag corrections near the stagnation point. Figure 4 presents the superposition of all instantaneous measurements of the lift coefficient for one test point. The repeatability is very good in the upstroke part of the cycle for which the flow remains attached, however when the sudden stall occurs, large discrepancies appear until reattachment.

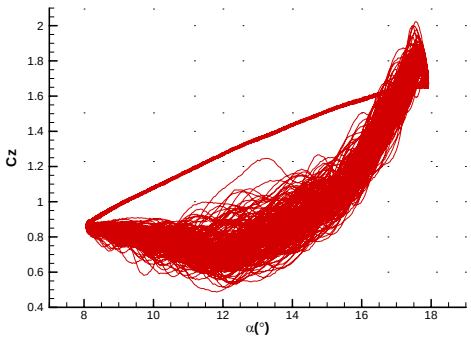

Figure 4: Example of instantaneous dynamic pressure measurement for a Deep Stall test point

For each test point, a post-processing is performed in order to get the mean value and standard deviation σ of the aerodynamic coefficients for each angle of attack. The final result is illustrated in figure 5. The error bars are representing the [-σ ; +σ] intervals. As observed on the instantaneous cycles, the repeatability is very good in the attached part, while discrepancies appeared in the detached part where the stall occurs. Such post-processing allows the discrepancies to be quantified and is very useful to compare the numerous test points acquired during the wind tunnel tests.

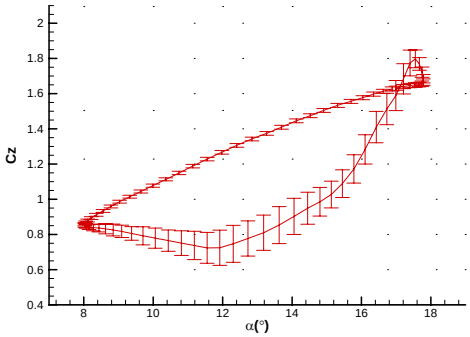

Figure 5: Result of dynamic pressure post-processing, averaged and standard deviation of the lift coefficient

Moderate and Deep stall configurations

A detailed parametric study over the nominal incidence, the amplitude and the reduced frequency of the pitching motion was performed to select two configurations presented in figure 6. The first is a "Moderate Stall" configuration (α_0=12° $\Delta\alpha$=5°). The second is a "Deep Stall" configuration (α_0=13° $\Delta\alpha$=5°).

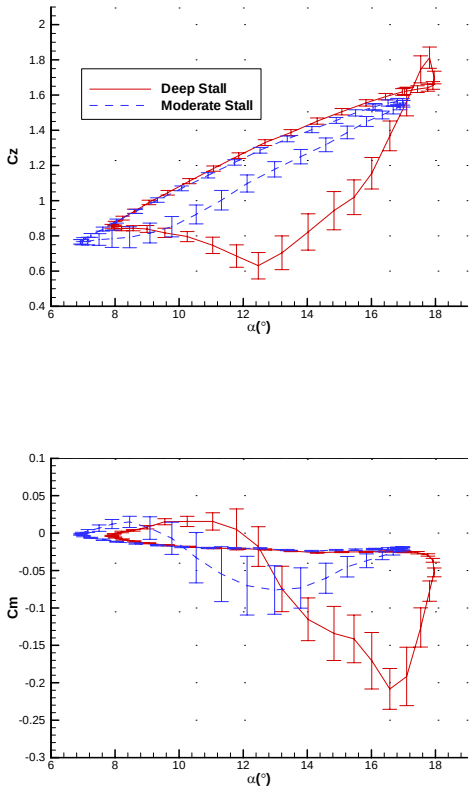

Figure 6: Reference "Moderate" and "Deep" Stall configurations

The difference in the pitching motion of the two configurations is only the mean value of the angle of attack. In Deep Stall configuration, the angle of maximum lift extends beyond the characteristic static stall angle. No change in the loading trend can be detected until a transverse vortex appears in the leading edge region. As the downstroke motion of the airfoil starts, the still developing vortex induces a stronger suction, which leads to a lift overshoot. When the vortex leaves the airfoil (while the downstroke motion is yet started) the lift suddenly decreases. The rearward movement of the vortex over the surface shifts the center of pressure; consequently, a large nose-down pitching moment is created. This event is often referred to as "moment stall" [1,5]. Then, vortex separation at pitch-down starts the hysteresis cycle. The flow remains separated over a great part of the oscillating cycle causing large hysteresis loops. When the boundary layer re-attaches, load and moment recover their quasi-linear evolution. In Moderate Stall configuration, lower angles of attack are reached, leading to a reduced lift hysteresis and a weaker negative pitch peak.

Repeatability

More than an hundred of test points were acquired during the campaign. In particular, numerous pressure measurements were performed on the two configurations "Moderate Stall" and "Deep Stall" during the LDV and PIV measurements in order to have a constant survey on the aerodynamic response of the model. Thus, 28 "Deep Stall" test points are plotted in figure 7, showing the very good repeatability over the wind tunnel test campaign that lasted more than 3 months.

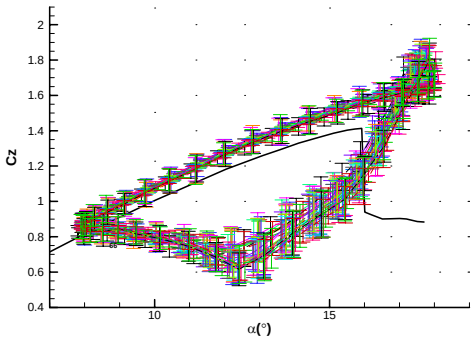

Figure 7: Repeatability over 28 Deep Stall test points - lift coefficient

Effect of the boundary layer transition

The effect of the boundary layer transition was also investigated by triggering the transition at x/c=3% on the suction side of the airfoil. The triggering was performed using a thin wire glued on the airfoil surface. The results on the lift and pitching moment coefficients for two wire thicknesses are presented in figure 8 for the Moderate Stall configuration.

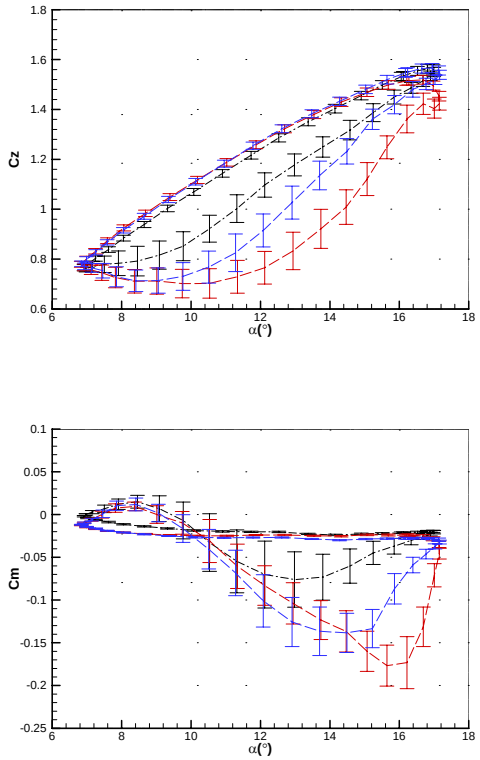

Figure 8: Effect of transition on the Moderate Stall configuration: Free transition (black), Triggered transition (red and blue for two different trigs)

This configuration was indeed found to be very sensitive to the test conditions. By triggering the laminar-turbulent transition, the stall phenomenon is much more pronounced and compares with a Deep Stall configuration. In particular, the negative pitching moment peak is much stronger.

The boundary layer detachment is so starting from the leading edge of the airfoil and mainly pilots the stall characteristic. This strong sensitivity is in good agreement with the sharp stall observed on the static polar of the lift coefficient above.

LDV measurements

In order to get information about the mean and turbulent velocity fields on the upper surface of the wing and in the wake, LDV measurements were undertaken.

Optical and mechanical setups

A 3D laser velocimetry bench was used. The three beams (green, blue and violet) come from two Spectra-Physics 171 argon laser, emitting 15 W all lines. The lateral horizontal arrangement chosen (figure 9) consists in emitting all the beams laterally on the left side of the test section. Two Cassegrain telescope are placed on the receiving part of the bench on the right side of the test section. The frequency shift which is induced on blue, green and violet component by acousto-optic modulators (Bragg cells) can be adjusted from 1 to 5 MHz. Flow seeding is done by incense smoke providing submicronic particles.

Figure 9: LDV arrangement

Data acquisition

Signals from the three photomultipliers and the shaft encoders are processed by a FSA 4000 from TSI. From the shaft encoder signals, FSA software generates a phase signal from 0° to 360° phase angle corresponding to an oscillating cycle of the wing. At each cycle, a pulse (corresponding to the nominal incidence angle) is delivered by an external pulse generator. Starting from this pulse, the TSI device creates its measurement window. At each oscillating cycle, data are recorded and dated relative to the beginning of the measurement acquisition window [6]. For each measurement point, 72,000 samples are recorded in a continuous way. In a post data processing, the acquisition window is separated into equal intervals that means 36 classes of 2000 samples available for mean average investigation. In each class, the three components of the velocity and all the components of the Reynolds stress tensor are computed.

A mesh of 3371 (Deep Stall) and 2575 measurement points (Moderate Stall) was defined (figure10).

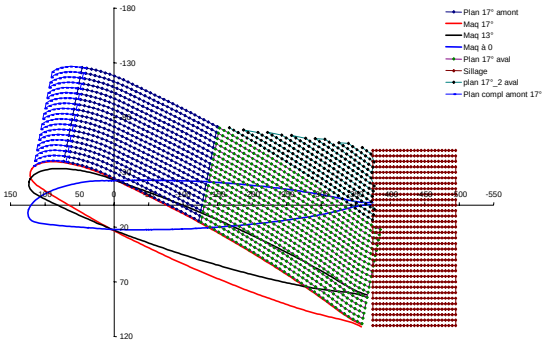

Figure 10: LDV measurement grid

Different measurement domains have been defined (to touch the laser beams again and) to take into account the occulted zones by the pitching airfoil.

Mean velocity field

Only results of LDV measurements referring to Deep Stall configuration are presented below.

When the incidence angle increases from nominal to maximum value, a quasi-steady flow pattern is present. The static-stall angle is exceeded and no particular sign of instability is perceptible on the wing. As soon as the pitch down movement starts, the first indications of stall are observed around x/c=25%. As the incidence decreases (figure 11a) a region of disturbed boundary layer flow moves quickly upstream. At α=17°, the boundary layer flow on the whole airfoil abruptly separates. Then, the magnitude of the reverse flow increases beyond the boundary layer flow (figure 11b). For further decreasing incidences (figure 11c) the boundary layer reattaches from the leading edge of the wing and the vortex shedding event is apparent. The dynamic stall phenomenon observed on a complete oscillating cycle can be summed up as a separation of the flow initiated with delay relating to the maximum incidence angle and that propagates all along the wing.

The analysis of the transverse velocity *W* is quite revealing of the complex nature of the dynamic stall. In the part of the oscillating cycle not affected by dynamic stall events, the flow can be considered as two-dimensional. As soon as first signs of stall appear, a sudden movement of the flow occurs in the spanwise direction (figure 12). Large transverse velocity changes are detected in an extended region from the leading edge. There is no longer any doubt regarding the three-dimensional character of the flow. The chaotic aspect of dynamic stall phenomenon should be probably retained.

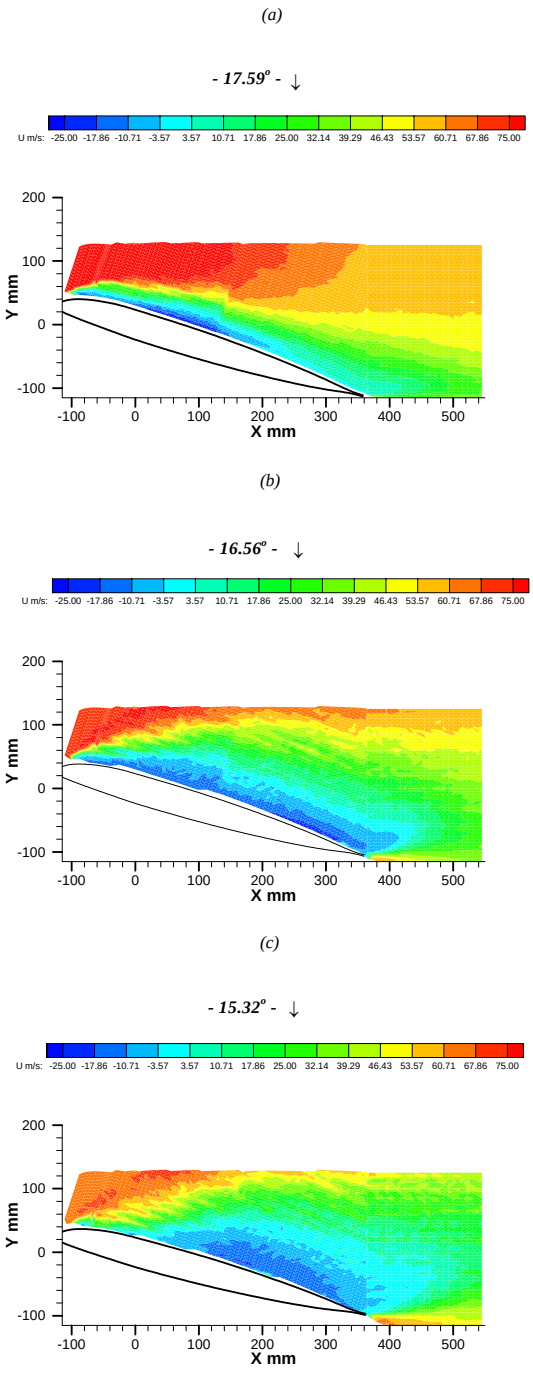

Figure 11: Mean velocity field – Streamwise U component – (↓: sign of downstroke motion)
- Deep Stall -

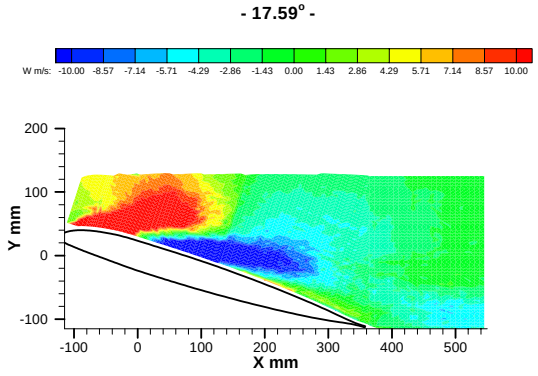

Figure 12: Mean velocity field – Spanwise W component –

Turbulent velocity field

In each class of recorded data, all the components of the Reynolds stress tensor were computed. To illustrate concisely the turbulent velocity field, only the evolution of the turbulent kinetic energy during the pitching motion of the airfoil is commented. When the incidence angle of the wing reaches its maximum value, a turbulence "pocket" originates in the boundary layer on the upstream part of the wing whereas the turbulence level notably increases. In the beginning of the downstroke part of the cycle, the turbulence extends on a large region (about two third of the upper surface) of the wing. As soon as the dynamic stall occurs, the boundary layer bursts and a separated flow takes place; the whole upper surface is concerned by high turbulence level (figure 13).

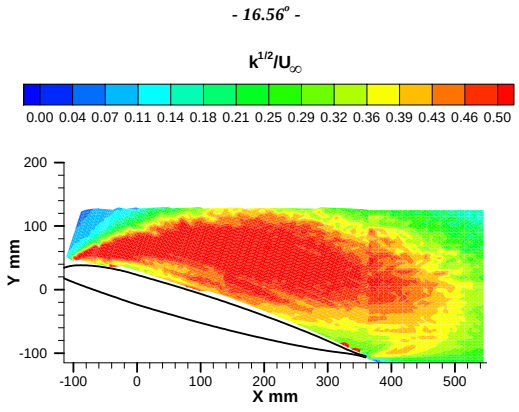

Figure 13: Turbulent velocity field – kinetic energy turbulence -

When the incidence angle becomes smaller than its mean value, the turbulence is swept away on the wing; turbulence recovers progressively its initial value from the leading edge toward the trailing edge and the wake. This evolution could be connected both with the formation and the propagation of vortex structures in the flow above the wing.

PIV measurements

Particle velocimetry system

The light source used was pulsed Nd:YAG laser with two independent oscillators. The pulse energy at 532 nm was 2x400 mJ. The Nd:YAG pulse laser was mounted on the top of the test section on the concrete foundations of the wind tunnel. The light sheet optics were mounted on the displacement bench of the set-up in order to be able to easily change the light sheet position. The digital SHARPVISION 1300 camera was located on the left side of the test section on the vertical part of the displacement bench. The flow was seeded with small olive oil droplets from a lazkinnozzle generator.

Operating procedure

From a pulse delivered by an external pulse generator at each oscillating cycle, the laser emits series of light impulses at a frequency range of 10.7 to 12.3 Hz containing the maximum processing frequency (11.7 Hz) of the PIV camera. The thermal equilibrium of the Yag cavities is attained at the end of the series of impulses and the recording of the pair of images is then authorized. The delay between the external pulse and the recording pulse signal must be chosen carefully in such a way that PIV recording be done in a continuous way. From the calculated delay, the recording pulse is generated by the second channel of the external pulse generator. Because of the fixed pulse rate of the laser and the low oscillating frequency of the model, it was not possible to record the flow field at many pitch angles during one oscillating cycle. The pulse recording was taken in successive cycles. A sequence containing 200 instantaneous velocity fields was collected at each of the twenty phase angles retained in the pitching cycle.

Instantaneous vorticity field

The optical access to the oscillating airfoil for the recording camera was reduced by the mechanical parts of the driving mechanism. So, PIV investigations could not have been performed upstream x/c=0.25. In spite of that, mean velocity

field measurements confirm the separation pattern attached to Deep or Moderate Stall configurations observed by LDV and described in the above paragraph.
The analysis of instantaneous velocity field (available in PIV only) relating to Deep Stall configuration shows that during the initial part of the cycle (α increases) vorticity marks are absent in a relatively quiet flow. When the incidence begins to decrease, this analysis reveals distribution of vortical structures propagating in the dynamic stalled flow far away from the airfoil. Figure 14 gives a picture of these vorticity events in dynamic stall configuration corresponding to figure 11b where the boundary layer flow is completely separated on the airfoil. The intensities of these local rotating region are estimated by computing the instantaneous vorticity of the velocity field. In a similar study [7], such localized vortices have been interpreted as being shed from the leading edge whereas the dynamic stall vortex was seen to separate from the airfoil.

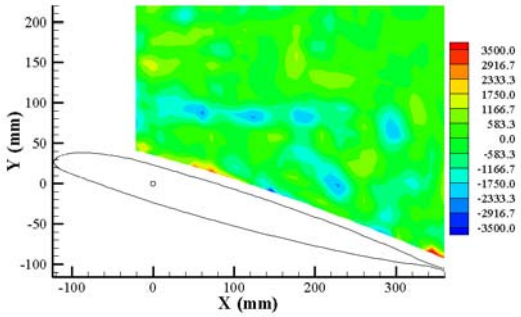

Figure 14: Instantaneous transverse vorticity field – Deep Stall – α =16.6° –

Skin friction measurements

Boundary layer features are quite difficult to capture by LDV or PIV measurements. So, skin friction measurements were undertaken to identify the dominant features in shear stress (on the upper side of the airfoil and particularly in the leading edge region) which could be related to dynamic stall events.

Calibration method

Quantitative analysis of skin friction requires a preliminary calibration of hot film sensors and skin friction gauges. The voltage through the wire or the film is related to the skin friction by:

$$\frac{E^2}{R\Delta T} = \frac{E_0^2}{R\Delta T} + B(\rho\mu\tau_w)^{1/3}$$

The 1/3 exponent comes from the theoretical analysis of a heat flux transferred to a fluid from a ΔT square pulse initiated at the wall. This 1/3 exponent is thoroughly confirmed in practice. However, the existence of a cavity under the fiber complicates the local geometry of the gauge and makes the mathematical model particularly approximate. So, an additional parameter is introduced in the calibration law:

$$\frac{E^2}{R\Delta T} = \frac{E_0^2}{R\Delta T} + B(\rho\mu\tau_w)^{1/m}$$

Now, the coefficients B and m must be determined by calibration. Generally, this calibration is undertaken in a special channel in which a steady turbulent flow is developed. Unfortunately, the gauges being implanted in the model, only an *in situ* calibration is possible. This calibration consists in recording the tensions delivered by the gauges in steady flow (the oscillating motion of the model is stopped) varying the incidence of the model and the reference velocity. The local values of skin friction (at gauge locations) are obtained from an ONERA boundary layer solver (3C3D) in which the imposed boundary conditions are provided with the measured pressure distribution on the airfoil. The computed skin friction is reliable even in transitional region except if a laminar separation occurs before transition. This situation may happen at low reference velocity, leading to an over-estimation of skin friction. The corresponding points are simply removed from the calibration process. An example of calibration results is given in figure 15. Determining the value of the exponent m and the B constant poses no particular problem. This is done by plotting the variation of the power dissipated by the fiber in the flow as a function of τ_w, in logarithmic coordinates. It is not easy to do an exhaustive analysis of the possible source of error. The uncertainty given in [8] relating to many calibrations in various configurations is about 3% in τ_w. In the present experiment, the local friction required for calibration was derived from calculation in a limited range of variation; so, it would be reasonable to consider the uncertainty in τ_w nearer 10% than 3%.

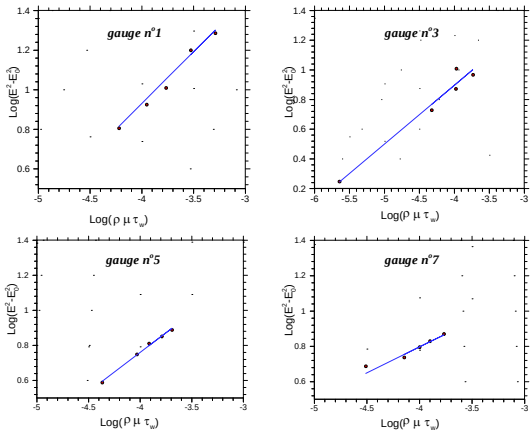

Figure 15: Example of calibration of skin friction gauges

Concerning the friction gauges, the principle of the friction measurement and the determination of its sign is particularly simple as the data from the two cold wires and from the hot fiber are uncoupled. The signals from the two cold wires and the hot fiber are digitized and the temperature of each wire is simply compared to a fixed threshold to determine the sign of the friction.

Skin friction from hot film sensors

For a better understanding of the phenomenon, most of the figures representing either the tension or the local friction coefficient emanating from hot film sensors and skin friction gauges include, in the upper part, the evolution in time of the incidence of the airfoil and its corresponding moment coefficient.

Deep Stall – Representative traces of the instantaneous values of local skin friction coefficient Cf_{local} are shown in figure 16.

Signals are plotted as a function of time and shifted each other of two units on *Cf* scale. It should be mentioned that we are not able, from such analysis, to distinguish between forward or reverse flow. Nevertheless, flow information can be obtained from the lecture of these signals. Near the leading edge (*x/c*=7%) the signal drops when the airfoil is at its minimum incidence angle.

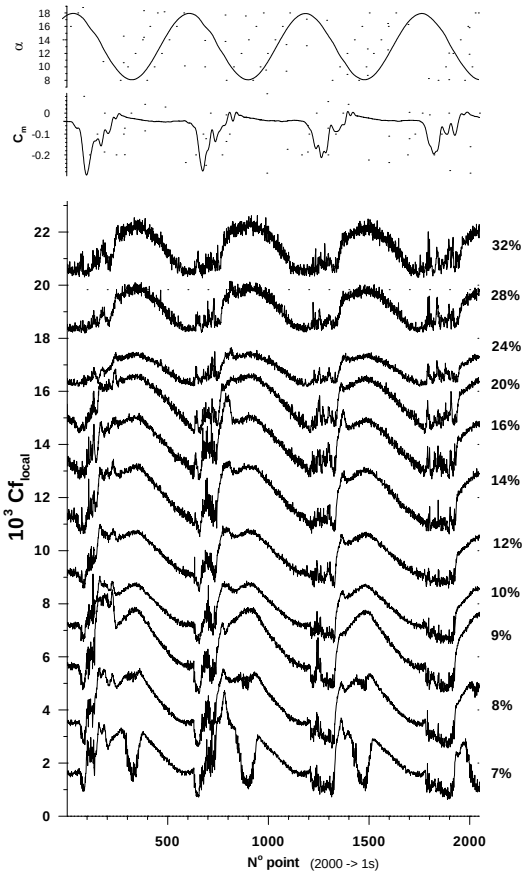

Figure16: Instantaneous skin friction coefficient

At the following measurement station (*x/c*=8%) this deficit on *Cf* value suddenly disappears. Probably the flow is already turbulent at the location of the first hot film and transition ended at moments corresponding to minimum incidence angle. Just when dynamic stall occurs in the oscillating cycle (as indicated by *Cm* evolution) the *Cf* signals related to all sensors exhibit a strong disturbance characterized by a high level of fluctuations. A cusp, fairly perceptible from *x/c*=7% to *x/c*=14%, is formed in a region dominated by large irregular fluctuations (around point 700 or 1400 in figure 16); this signal behavior could normally be indicative of development of vortex flow.

The phase averaged evolution of the root mean square value of the local friction coefficient (figure 17) reveals a separation of the flow well connected to dynamic stall event. Separation is detected by a distinct increase of the rms value of the skin friction coefficient. The maximum of the rms value is shifted with *x* during an oscillating cycle. These observations might open a credit to the formation of a vortex-like disturbance in the leading edge region and to its propagation along the upper surface of the wing.

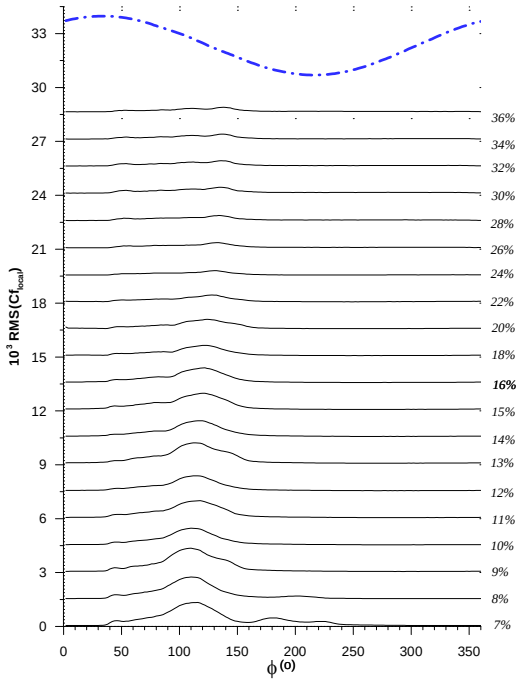

Figure 17: Rms value of the skin friction coefficient in Phase averaged representation

Moderate Stall – The moderate stall phenomenology was previously illustrated by the evolution of unsteady load and moment. The loops formed by the plot of the section coefficients versus angle of attack exhibit a hysteresis character of lesser importance than in deep stall configuration. Flow separation on the upper surface of the wing might be damped. The evolution of the local friction coefficient versus time (figure 18) reinforces this hypothesis. The signal is not much more affected at the instant of the dynamic stall than at any other instant of the oscillating cycle. On the two first investigated stations (7% and 8%) the laminar nature of the boundary layer for the lowest value of the pitch angle is not questionable. Downstream, up to *x/c*=11%, transition occurs and the signal exhibits locally high fluctuations. Anywhere else, the signal shows small fluctuations, indicating that transition already tooks place probably before *x/c*=7%. At this stage of the analysis, we are in a position to think that transition interferes according to a regular process corresponding to a periodic displacement of the point of beginning of transition between *x/c*=5% and *x/c*=12% with separation bubble.

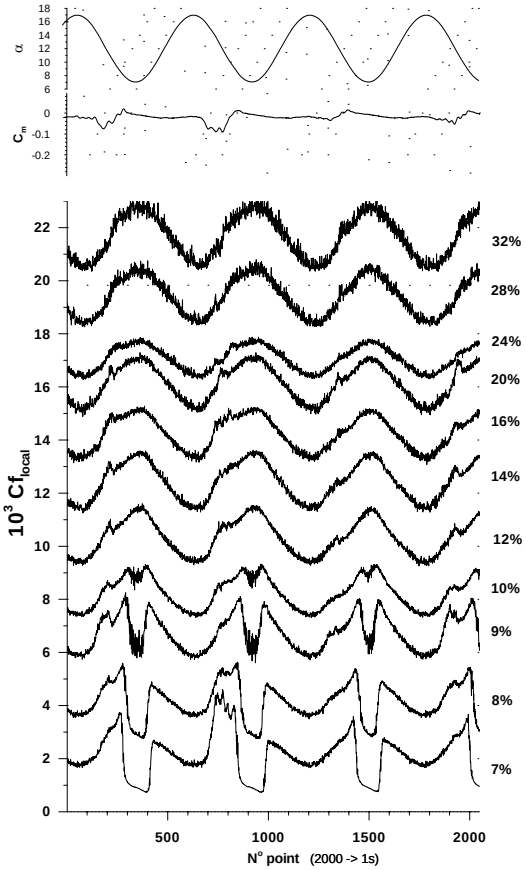

Figure18: Instantaneous skin friction coefficient -Moderate Stall-

Skin friction from 3 wires gauges

Essential flow features are present in the local skin friction signal emanating from the calibrated hot film sensors. The meaning of some particularities on *Cf* signal can be easily linked, for example, to transition onset or transition front movement. In return, a laminar separation bubble or a separated flow region can be suspected but not detected. Skin friction gauges aids in this effort. An example of signals delivered by the two cold wires and the hot fiber is given in figure 19. It can be noted that the two cold wire signals are in phase opposition. The red dashed line corresponds to a possible threshold that could be applied to cold wire signal.

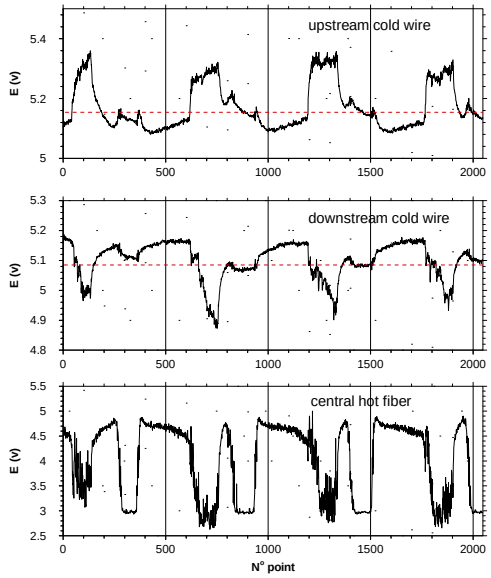

Figure 19: Three wires gauge signals

Deep Stall - Figure 20 presents the skin friction evolutions obtained, after calibration, from the signals of the nine gauges located from *x/c*=5% to *x/c*=85%. Signals are shifted each other of 0.010 on *Cf* scale. The zero-friction level affected at each plot is marked with a horizontal dotted line.

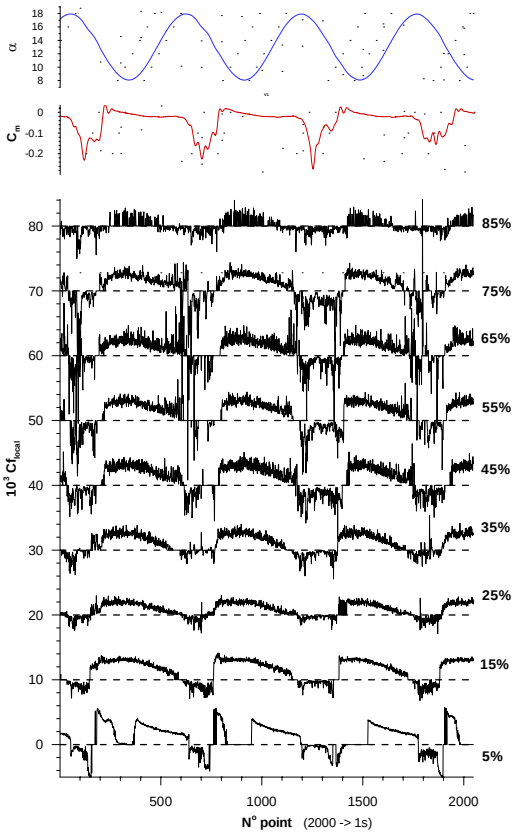

Figure 20: Instantaneous skin friction coefficient -Deep Stall-

Slight disturbances appear on *Cf* distribution at the first measurement station indicating that transition is already effective at *x/c*=5%. At moments of minimum incidence angle the boundary layer remains laminar; the skin friction is very close to zero. The sudden breakdown of the signal (at moment corresponding to dynamic stall) associated to peculiar peaks and high frequency fluctuations towards negative *Cf* values, could be understood as a sign of the mechanism of laminar bubble bursting. From *x/c*=15%, the signal exhibits a quasi-periodic behavior with negative values connected to dynamic stall event. Flow separation occurs probably before *x/c*=5% but massive separation takes place from *x/c*=35% as indicated by the high amplitude of friction fluctuations.

The mean friction coefficient (figure 21) was obtained from the average of 300 sets of 2048 samples. The periodic aspect of the signal is noteworthy. Flow reversal region in the oscillating cycle is precisely defined and coincides clearly with dynamic stall event. The fluctuations present in the signal at the last investigated stations confirm the strong effect of the dynamic stall on the flow developing in the rear part of the airfoil.

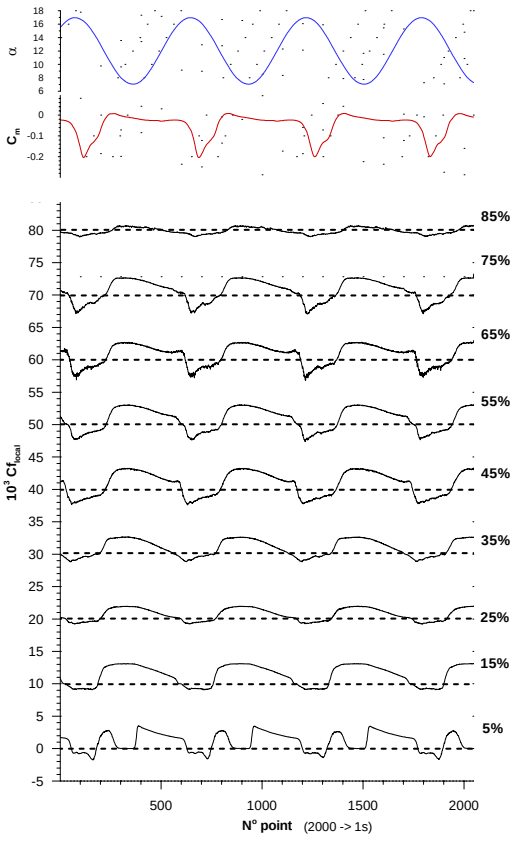

Figure 21: Mean friction coefficient

Figure 22 shows cycle average pattern of local skin friction coefficient. One period of oscillation cut in pitch cycle phase angles equally spaced is shown in every trace. Skin friction traces have quite

similar behavior. Presence of dynamic stall event is marked by a “pocket” of negative friction spreading over more than a quarter of the oscillation period. From the evolution (versus x) of the phase angle where the skin friction begins to increase from zero value, it can be assumed that the dynamic stall vortex propagates on the upper surface of the wing at about a velocity of $0.30U_0$.

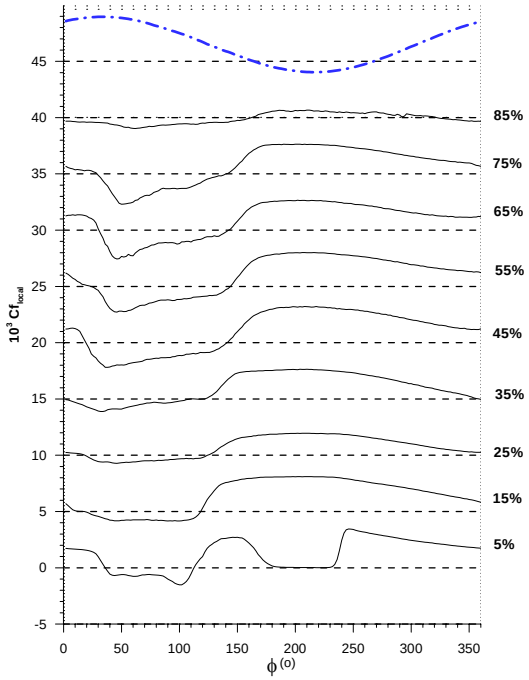

Figure 22: Phase averaged skin friction

Moderate Stall – A definite answer about the presence or not of a laminar separation bubble in transition process, evoked at the time of hot film signals analysis, cannot be provided here. In fact, the spacing between the skin friction gauges in the leading edge region is larger than the distance corresponding to transition onset. Nevertheless, it can be confirmed (figure 23) that transition occurs at x/c=5% in the whole oscillating period except at moments of minimum incidence angle during which the flow, characterized by a weak but positive friction coefficient, is well laminar. Disturbance observed on the first hot film signal (between point N° 700-800 in figure 18) can now be identified as hazardous incursion of dynamic stall in the leading edge region. As in deep stall case, dynamic stall effect on the rear part of the wing is characterized by high negative fluctuation of the skin friction coefficient.

The plots of mean skin friction coefficient (figure 24) clearly indicate that if dynamic stall effects are perceptible in the leading edge region, flow reversal concerns essentially the rear part of the wing from x/c=35%.

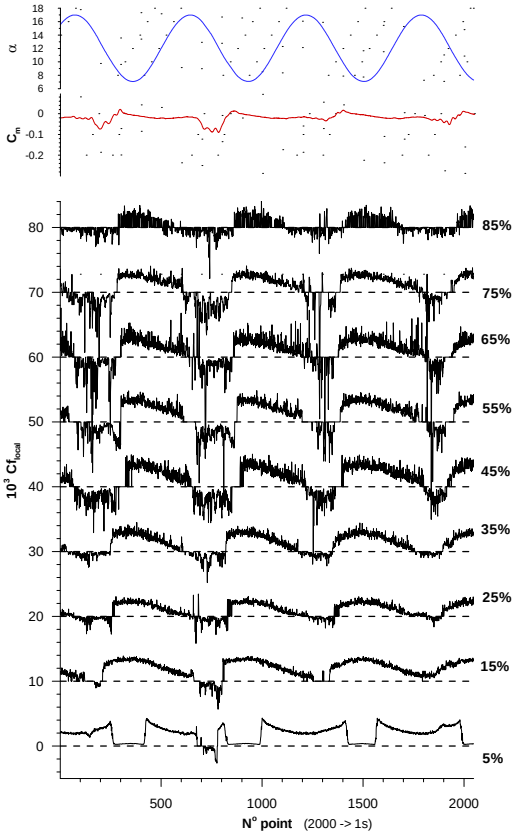

Figure 23: Instantaneous skin friction coefficient – Moderate Stall –

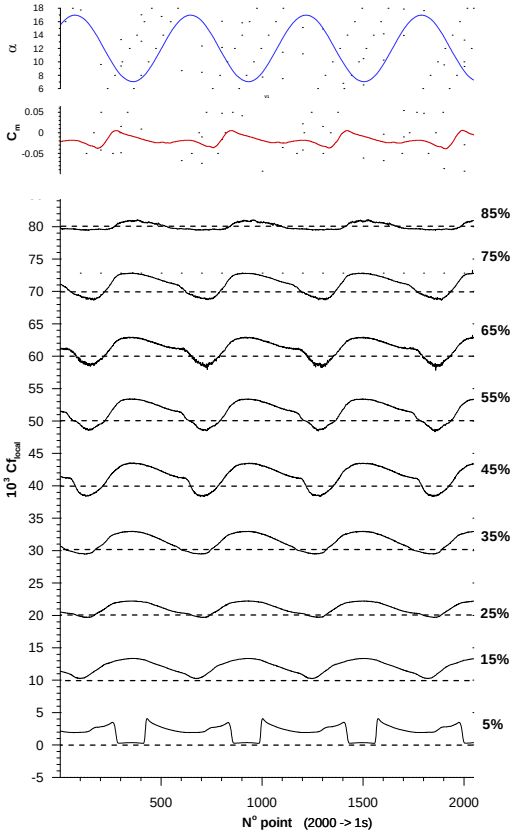

Figure 24: Mean skin friction coefficient – Moderate Stall –

Conclusion

This experimental study was conducted to investigate the unsteady flow field above an OA209 airfoil pitching under dynamic stall conditions. The airfoil model was instrumented with pressure sensors, hot films sensors and three wires friction gauges. Unsteady loads and moments were measured varying the nominal incidence angle, the amplitude of incidence and the frequency of the oscillating movement. Finally, a Deep and Moderate dynamic stall configurations were chosen and detailed. An analysis of the repeatability of unsteady loads and moments measurements coupled with an evaluation of their discrepancies showed a relative reliability of the experiment. The flow field has been documented using both time and phase averaging technique in LDV and PIV measurements. Dynamic stall can be depicted as a separation of the flow initiated in the leading edge region and which spreads on the whole surface of the wing. Vortex shedding phenomenon forming on the suction surface appears to be the significant feature of dynamic stall. This vortex shedding seems probably connected to the unsteady motion of the flow drastically initiated in spanwise direction during a part of pitching cycle dominated by stall effect. A part of our efforts was focused on the measurement of skin friction on the upper surface of the wing where a strong detached flow develops. Hot film sensors and friction gauges used with calibration provided an accurate description of the changes in shear stress related to dynamic stall events.

A large part of the database obtained in this experiment remains to be analyzed in particular the turbulent velocity field from LDV and the instantaneous vorticity field from PIV measurements. This database will be completed with results emanating of last just ended experiment in which the Reynolds number effect has been tested.

Acknowledgment

The authors would like to thank all DMAE people interested in test preparation and all the F2 wind tunnel people involved in this experiment.

References

[1] Carr L., Mc Alister K., Mc Kroskey W.: *Analysis of the development of dynamic stall based on oscillating airfoil experiments*, NASA Technical note, NASA TN D-8382, 1977

[2] Piziali R. A.: 2-D and 3-D oscillating wing aerodynamics for a range of angles of attack including stall, NASA Technical M. 4632, USAATCOM Technical Report 94-A-011, Sptember 1994

[3] Ham N.D.: *An experimental investigation of stall flutter*, Journal of American Helicopter Society, vol.7, N1, January 1962

[4] Mc Croskey J., Fisher R.K.: *Detailed aerodynamic measurements on a model rotor in the blade stall regime*, Journal of American Helicopter Society, vol.7, N1, January 1972

[5] Weaver D., Mc Alister K., Tso J.: *Suppression of dynamic stall by steady and pulsed upper-surface blowing*, NASA Technical Paper 3600, ATCOM Technical Report 95-A-005, February 1996

[6] Boutier A., Lefèvre J., Micheli F.: *Analysis of helicopter blade vortex structure by laser velocimetry*, Experiments in Fluids, 21 (1996) pp 33-42

[7] Raffel M., Kompenhams J., Wernert P.: *Investigation of the unsteady flow velocity field above an airfoil pitching under deep dynamic stall conditions*, Experiments in Fluids, 19 (1995) pp 103-111

[8] Houdeville R., Juillen J.C., Cousteix J.: *Skin friction measurements with hot-element gauges*, Recherche Aérospatiale, 1984-1